metals

MDPI

Article

Numerical Simulation of Densification of Cu–Al Mixed Metal Powder during Axial Compaction

Wenchao Wang, Hui Qi, Pingan Liu *, Yuanbo Zhao and Hao Chang

College of Aerospace & Civil Engineering, Harbin Engineering University, Heilongjiang 150001, China; 18846839308@163.com (W.W.); qihui205@sina.com (H.Q.); ZYB201507@126.com (Y.Z.); changxiaohaoheu@163.com (H.C.)

* Correspondence: liupingan631@163.com; Tel.: +86-131-0450-6106

Received: 26 June 2018; Accepted: 5 July 2018; Published: 12 July 2018

Abstract: The densification mechanism of Cu–Al mixed metal powder during a double-action die compaction was investigated by numerical simulation. The finite element method and experiment were performed to compare the effect of the forming method, such as single-action die compaction and double-action die compaction, on the properties of compact. The results showed that the latter could significantly raise the densification rate and were in good agreement with Van Der Zwan–Siskens compaction equation. The effects of the different initial packing structures on the properties of the compact were studied. The results showed that a high-performance compact could be obtained using a dense initial packing structure at a given compaction pressure. Additionally, the effects of the Al content and compaction pressure on the relative density and stress distribution were analyzed. It was observed that, with an increase in the Al content at a given compaction pressure, the relative density of the compact increased, whereas the stress decreased. Furthermore, when the Al content was fixed, the relative density and stress increased with increasing compaction pressure. The relationship between the relative density and the compaction pressure under different friction conditions was characterized and fitted according to the Van Der Zwan–Siskens compaction equation. The influence mechanisms of die wall friction on the compaction behavior were investigated. It was revealed that friction is a key factor that causes the inhomogeneity of the powder flow and stress distribution. Finally, the effects of the dwell time and height–diameter ratio on the densification behavior were analyzed, and it was found that an increase in the dwell time promoted the densification process, whereas an increase of the height–diameter ratio could hinder the process.

Keywords: powder metallurgy; densification mechanism; compaction equation; friction

1. Introduction

As a result of the excellent anti-corrosion performance, high abrasion resistance, and other thermoelectric properties of Cu-based metal matrix composites, they have a wide range of engineering applications, for example, in the manufacture of connectors, heat exchangers, and piping [1]. These composites are incorporated with different metal elements, such as Al, Be, and Ni, in various proportions in order to improve the mechanical properties [2,3]. Al is the most widely used metal in the industry, therefore, Cu–Al alloys are one of the most typical alloys, which have been employed in many studies [4–7]. For instance, aluminum bronze is a kind of Cu-based alloys that is synthesized using different compositions of Al powder [8,9]. Cu–Al alloys have been used extensively in automotive, aerospace, electronic, and machine tool industry [10]. They are reported to possess good mechanical performance, high strength, and high temperature resistance properties [11–14]. On account of the high melting point of Cu–Al alloys, their synthesis by methods, such as smelting and casting, are complicated. Therefore, the conventional powder metallurgy process, which includes the processes

of cold compaction and sintering, is used to synthesize Cu–Al alloys [15,16]. Cold compaction is an important procedure in the manufacture of compacts with excellent performance, high efficiency, and low cost [17]. The powder forming process directly influences the density and homogeneity of the green compact, both of which, in turn, affect the uniformity of volume shrinkage in the subsequent sintering process. The compaction process can be roughly divided into three steps, namely die filling, powder compaction, and ejection. Researchers have thus far focused mostly on the powder compaction step, and die filling, despite being an essential step of the compaction process, has rarely been studied in the past.

The friction between the powders and the die wall during the powder compaction process has significant influence on the properties of the compact, such as the powder flows, relative density, and stress distribution. An et al. [18] analyzed the copper powder flow in the axial and radial direction under the influence of friction. Zhou et al. [19] examined the effects of friction on the properties of the compacts and rules of powder flow under different friction conditions. However, such previous studies focused mainly on the rules of the powder flow in single-action die compaction, in which the relative density gradient is significant and the distribution is heterogeneous. This can be conquered by the double-action die compaction, whose analysis is less systematic. Furthermore, the dwell time is regarded as a critical factor in the actual production, but has been neglected in most of the theoretical analyses. Consequently, it is important to examine the powder behavior and the influence mechanisms of the dwell time in the compaction process.

In the present study, numerical analyses were performed to identify the double-action die compaction behavior of Cu–Al mixed metal powders. The relationship between the average relative density and the compaction pressure, in the case of loose and dense initial packing structures with different Al contents, was first discussed. The relative density and the stress distributions in the powder compact under different Al contents, compaction pressures, and friction conditions were characterized. Different compaction equations were studied and compared to propose a suitable compaction that included the effects of the die wall friction, with the aim of characterizing the compact properties at different compaction pressures. The influence mechanisms of friction were analyzed in detail. Finally, the influence of dwell time was analyzed to elucidate its influence on the compaction behavior.

2. Materials and Methods

2.1. Materials

Commercial pure Cu (99.9% purity, mean particle size <50 μm, 325 mesh) and Al (99.9% purity, mean particle size <50 μm, 325 mesh) powders were used in the compaction work. All of the metal powders were supplied by Hebei Nangong Zhongzhou Alloy Material Ltd., Xingtai, China. As shown in Figure 1, the morphology of the powders was characterized by scanning electron microscopy (SEM). The Cu and 30 pct (mass fraction) Al composite powders were dry blended using a blender mixer at a rotation speed of 20 rpm for 9 hours. The die wall was lubricated using a commercial lubricant, Zinc stearate, which was mixed with alcohol and daubed onto the die wall to reduce the die wall friction.

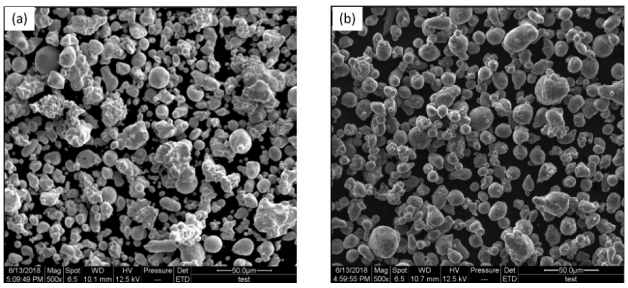

Figure 1. The morphology of (**a**) Cu powders and (**b**) Al powders.

2.2. Experiments

The Cu–Al mixed metal powder were compacted in a 20 mm diameter cylindrical die at room temperature. A hydraulic universal testing machine was used to control the loads applied on the punches during the process of compaction. For each compaction experiment, 41 g of mixed metal powders were poured into the die. The initial height of the filling powder is about 40 mm, and according to the density formula, the initial packing density can be calculated as the total mass of the filling mixed metal powder divided by the volume occupied by those powders. Figure 2 shows the schematic drawing of the compaction experiments. During the single-action die compaction, pressure was applied on the upper punch and the upper punch moved downward to press the powder, while the die and bottom punch remain stationary. During the double-action die compaction, pressure was applied on both the upper punch and bottom punch. In the compaction, the loading speed was set as 2 mm/min, and the compacts were loaded to a certain pressure and then maintained the pressure for 15 min.

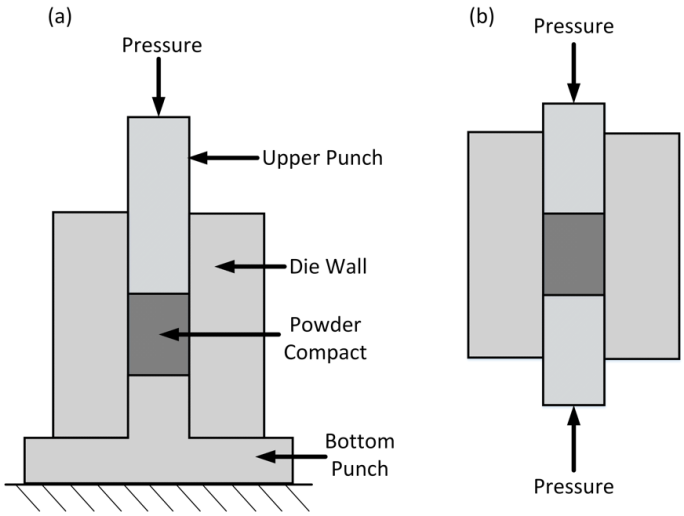

Figure 2. Schematic diagrams of (**a**) single-action die compaction and (**b**) double-action die compaction.

The average density of each green compact was measured by the mass and its volume. A precision mass balance was used to weigh the green compacts after being ejected from the die. The volume of the green compacts was calculated as the average cross-sectional area multiplied by its height. In addition, a Vernier caliper was used to measure the diameter and height of each compact. The measurements of each compact repeated at least five times and took the average. The measurement procedures are similar to Lou's work. The average relative density was obtained by the ratio of the average density to the theoretical density of the mixed metal powder, which is the maximum value of the compact.

2.3. Finite Element Model and Simulation Conditions

Researchers began studying the yield criteria and forming a theory of powder materials around 1970. Shima and Oyane [20], Kuhn and Downey [21], and Doraivelu et al. [22] constructed different forms of yield functions based on the Von Mises yield criterion, by taking into account the influence of hydrostatic stress. These yield criteria are of a similar form, which is expressed as follows:

$$F = AJ_2' + BJ_1^2 - \delta\sigma_S^2 = 0 \quad (1)$$

where F is the yield function, J_1 and J_2' are the stress invariant and second deviatoric stress invariant, respectively. σ_s is the yield limit of dense metal, and A, B, and δ are the model parameters, which are the function of relative density. The mechanical properties of the compact are consistent with those of

the dense metal when the material is compacted completely. Therefore, some conditions need to be specified, as follows:

$$\begin{cases} \lim\limits_{\rho\to 1} A = 3 \\ \lim\limits_{\rho\to 1} B = 0 \\ \lim\limits_{\rho\to 1} \delta = 1 \end{cases} \tag{2}$$

Thus, this yield condition tends to the von Mises yield criterion for the dense metal when the relative density approaches 1.

Finite element (FE) simulations of the double-action die compaction of the Cu–Al mixed metal powders were performed with MSC.Marc 15.0 FE software (MSC Software, Newport Beach, CA, USA). In the modeling, it is crucial to select an appropriate material model for representing the behavior of the powder particles. In the present study, the modified Shima model, an intrinsic module in this software, was used as the material model; in this model, the yield function of this material is a function of the relative density. The equation of this model is given as follows:

$$F = \frac{1}{\gamma}\left(\frac{3}{2}\sigma^{\mathrm{d}}\sigma^{\mathrm{d}} + \frac{p^2}{\beta^2}\right)^{\frac{1}{2}} - \sigma_y \tag{3}$$

where σ_{y} is the uniaxial yield stress, σ^{d} is the deviatoric stress tensor, p is the hydrostatic pressure, and γ and β are the material parameters. σ_{y} is a function of the temperature and relative density, and γ and β are functions of the relative density. γ and β are, respectively, given as,

$$\begin{aligned} \gamma &= \left(\mathrm{d}_1 + d_2\rho^{d_3}\right)^{d_4} \\ \beta &= \left(\mathrm{b}_1 + b_2\rho^{b_3}\right)^{b_4}. \end{aligned} \tag{4}$$

For Cu, Al, and Fe,

$$\begin{aligned} \gamma &= \rho^{2.5} \\ \beta &= (5.9 - 5.9\rho)^{-0.514} \end{aligned} \tag{5}$$

it can be seen that γ and β are functions of the relative density ρ, which is a state variable and can be defined as follows:

$$\rho = \rho_{\mathrm{c}}/\rho_t \tag{6}$$

here, ρ_{c} is the current density of the powder compact, and ρ_t is the theoretical density. The theoretical density of a mixed metal powder can be calculated according to the mass fraction of each kind of powder by the equivalent density method, as follows:

$$\rho_t = \frac{m_{total}}{V_1 + V_2 + \cdots V_n} = \frac{m_{total}}{\frac{m_1}{\rho_1} + \frac{m_2}{\rho_2} + \cdots \frac{m_i}{\rho_i}} \tag{7}$$

$$m_{\mathrm{i}} = f_{\mathrm{i}} m_{total} \tag{8}$$

where m_i and V_i are the mass and volume, respectively, of powder i, and f_i and ρ_i are the mass fraction (wt %) and theoretical density, respectively, of powder i [23].

According to the Han et al. [24], the Young's modulus of a Cu–Al composite dense body can be calculated by the following expression:

$$E_{\mathrm{c}} = E_{\mathrm{Cu}}\nu_{\mathrm{Cu}} + E_{Al}\nu_{Al} \tag{9}$$

where E_c, E_{Cu}, and E_{Al} are the Young's modulus of the compact, Cu, and Al, respectively. ν_{Cu} and ν_{Al} are the volume fractions of Cu and Al, respectively, and $\nu_{\mathrm{Cu}} + \nu_{Al} = 1$. The yield strength of the Cu–Al composite dense body is given as follows:

$$\sigma_c = \sigma_{Cu}\nu_{Cu} + \sigma_{Al}\nu_{Al} \tag{10}$$

where σ_c, σ_{Fe}, and σ_{Al} denote the yield strengths of the compact, Cu, and Al, respectively. In this study, the Young's modulus and yield strength of Cu and Al are taken as E_{Cu} = 125 GPa, $\sigma_{\mathrm{Cu}} = 200$ MPa, and, E_{Al} = 62.59 GPa, $\sigma_{\mathrm{Al}} = 60$ MPa, respectively. Therefore, the Young's modulus and yield stress of the Cu–Al incompressible composite can be calculated by Equations (9) and (10), respectively. According to the empirical formula proposed by McAdam and study of Kuhn et al., the Young's modulus and yield strength of a powder material are related to the corresponding dense body and given by the following:

$$E = E_c\rho^{3.4} \tag{11}$$

$$\sigma = \rho^n\sigma_{\mathrm{c}} \tag{12}$$

According to the research by Zhdanovich, the Poisson's ratio is a function of the relative density and can be expressed as follows [25]:

$$\upsilon = 0.5\rho^n \tag{13}$$

According to the research by Kuhn et al. [21], for cold compaction, n = 1.9.

In an FE simulation, a three-dimensional (3D) cylindrical geometric model with a rigid surface can represent the compaction process of Cu–Al mixed metal powders. In order to represent the compaction process clearly, a 1/4-cylinder model was used in the present study, as shown in Figure 3. Different mesh sizes of the powder compact and different punches were designed to investigate the sensitivity of the FE simulation results to the mesh size.

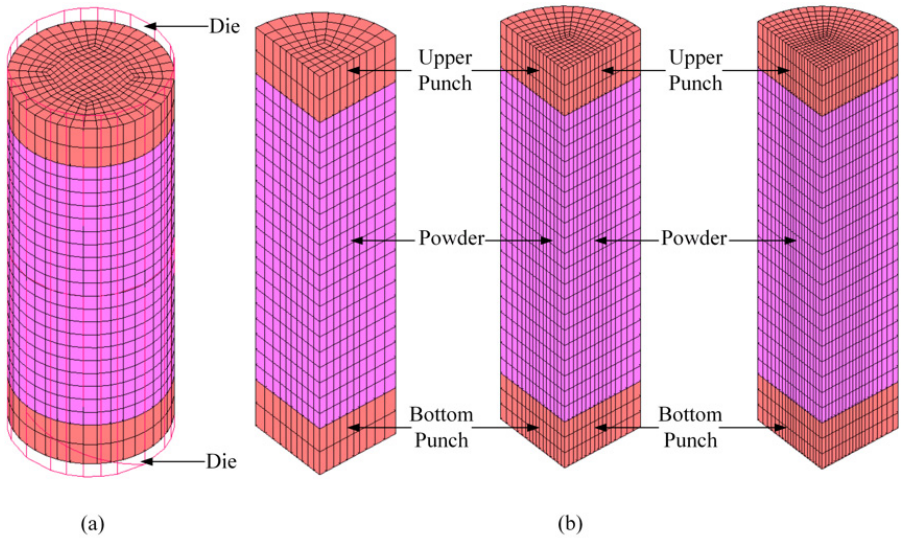

Figure 3. (**a**) Schematic of three-dimensional (3D) finite element (FE) model and (**b**) a $\frac{1}{4}$-cylinder model with different mesh sizes.

In the 3D geometric model, the upper punch and bottom punches, which have large stiffness, can be regarded as rigid bodies, and the powders are deformable. The initial height of the mixed powders in the die is 40 mm, and the diameter is 20 mm. The apparent density is defined as the spontaneous stacking density of the powders, which depends on the adhesive force, relative sliding resistance, and the degree of filling in the interspace. The knock and vibration can improve the particle rearrangement

and increase the stacking density [17]. In order to analyze the influence of the apparent density on the relative density of the compact, two different initial relative densities, 0.56 and 0.62, are considered in this simulation. The former value corresponds to natural stacking without any vibration or knock, and an inhomogeneous distribution of voids. The latter value corresponds to the condition wherein the powders are subjected to continuous mechanical vibration, as a result of which the distribution of the packing density is uniform. In all of the simulations, the friction coefficient between the powder and die wall was taken to be equal to both the friction coefficient between the powder, and the upper punch and the friction coefficient between the powder and the bottom punch, and this friction coefficient was treated as a constant. In order to study the effects of die wall friction, different die wall friction coefficients for lubricated and unlubricated were modeled. In addition, the effects of the Al content, compaction pressure, and dwell time on the compact performance were also simulated.

2.4. Compaction Equations

The compaction equations provide an effective and easy method for predicting the density of a powder compact at a given compaction pressure. Several previous studies proposed different empirical compaction equations, as specified below.

Heckel [26] proposed the following:

$$\ln[1/(1-\rho)] = A_1 P + B_1 \tag{14}$$

Huang et al. [27] proposed the following:

$$\lg P = A_2 \lg \ln \frac{(\rho_m - \rho_0)\rho}{(\rho_m - \rho)\rho_0} + B_2 \tag{15}$$

Balshin [28] proposed the following:

$$1/\rho = A_3 \ln P + B_3 \tag{16}$$

Here, P represents the compaction pressure, ρ is the relative density of the powder compact, ρ_m is the theoretical density of the Cu–Al mixed metal powder, and ρ_0 is the initial relative density. A_1, A_2, and A_3 are the hardening exponents, B_1, B_2, and B_3 are the constants [29].

Van Der Zwan and Siskens [30] proposed the following:

$$\frac{\rho - \rho_0}{\rho(1-\rho_0)} = A_4 \exp(\frac{B_4}{P}) \tag{17}$$

where A_4 is the rate of the plastic deformation coefficient, and B_4 denotes the magnitude of the pressure at which the plastic deformation begins. The above-listed compaction equations were employed to study the relationship between the compaction pressure and the relative density under different die wall friction conditions.

3. Results and Discussion

3.1. Effects of Apparent Density of Mixed Powder and Al Content on Powder Compact

The relative density distributions of the compacts with three different mesh sizes, depicted in Figure 3b, is shown in Figure 4 to evaluate the mesh sensitivity at a compaction pressure P = 200 MPa and Al content is 30 wt %. A comparison of the relative densities for the different nodes with different incremental modeling steps is shown in Figure 5. It can be seen that the changes in the relative density at the same position in the powder compact were less than 1%, indicating that the simulation results were insensitive to the mesh size. Therefore, the mesh shown in Figure 4a was used in the subsequent FE simulations.

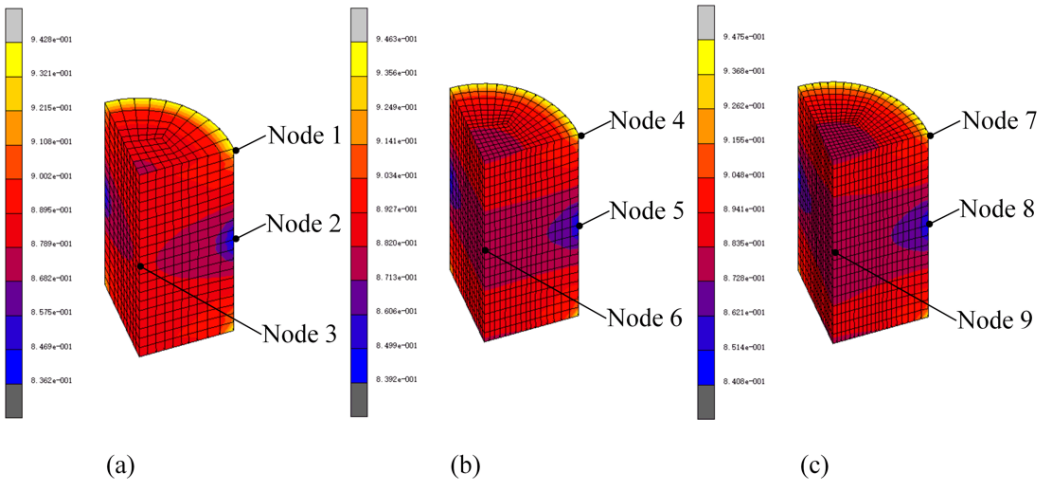

Figure 4. Comparison of relative density distributions for different mesh sizes. (**a**) sparse mesh, (**b**) general mesh, (**c**) dense mesh.

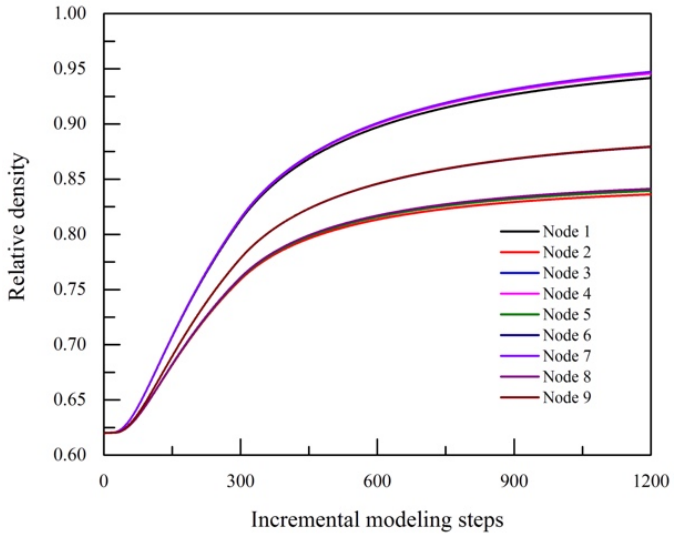

Figure 5. Variation of the relative density with incremental modeling steps for nine nodes.

A variation of the average relative density with compaction pressure for simulation and experiment was shown in Figure 6. It can be observed that the simulation results are in accordance with the experimental measurements both for the single-action die compaction and double-action die compaction, indicating that the model could be used to describe the compaction behavior for the Cu–Al mixed metal powder. As it can be seen, the average relative density of the compact increases and then trends to be flat with increasing compaction pressure. In addition, the average relative density in a double-action die compaction is higher than that in a single-action die compaction. Figure 7 shows some of the specimens fabricated in the experiments. The curves of simulation and experiment are fitted with the different empirical compaction equation mentioned in Section 2.4 and the fitting parameters are listed in Table 1. A comparison and analysis of the regression coefficients reveals that the Van Der Zwan–Siskens compaction equation shows the best regression. Hence, this compaction equation can be employed to quantitatively analyze the relationship between the relative density and the compaction pressure.

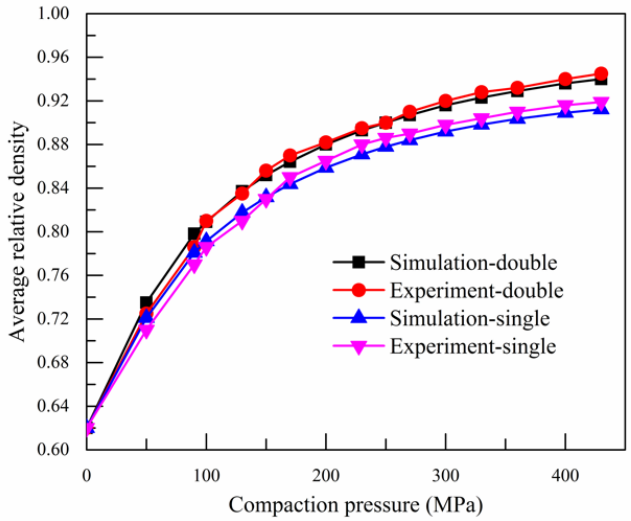

Figure 6. Variation of average relative density with compaction pressure for simulation and experiment.

Table 1. Fitting parameters of compaction equations for simulation and experiment.

Conditions		Heckel Equation			Huang Equation		
		A_1	B_1	R^2	A_2	B_2	R^2
Simulation	Double-action	0.00378	1.30137	0.97436	1.52294	2.05193	0.98787
	Single-action	0.00292	1.3023	0.94952	1.57587	2.14504	0.97542
Experiment	Double-action	0.00406	1.25815	0.97312	1.39128	2.07034	0.98021
	Single-action	0.00328	1.24988	0.94236	1.38011	2.15883	0.96869
Conditions		**Balshin Equation**			**Van Der Zwan–Siskens Equation**		
		A_3	B_3	R^2	A_4	B_4	R^2
Simulation	Double-action	−0.13365	1.85538	0.97712	0.97746	−43.75487	0.99769
	Single-action	−0.13155	1.87319	0.97431	0.92471	−45.71933	0.99754
Experiment	Double-action	−0.14395	1.90943	0.96719	1.0068	−49.6389	0.99584
	Single-action	−0.14731	1.955	0.96683	0.9732	−54.88447	0.99572

Figure 7. The Cu–Al 30 wt % mixed powder compact specimens.

The difference in the average relative density of the compact obtained by the single-action and double-action die compaction is mainly because of the difference in the local relative density. One of the biggest benefits of FEM is that it can accurately simulate the actual operating state, partially substitute, and guide the experiment, for example, FEM can quantitatively characterize the distribution of the relative density under different compaction conditions to provide a reference for the optimization of the compaction process and prevent possible defects. Figure 8 shows the relative density distributions in the powder compacts produced by a single-action die compaction and a double-action die compaction

with an Al content of 30 wt % and a compaction pressure P of 200 MPa. It can be seen that the maximum relative densities are nearly equal in both of these cases, whereas the minimum relative density in the double-action die compaction is higher than that in the single-action die compaction. The latter result confirms that the double-action die compaction can help to improve the density homogeneity of the powder compacts, this is because the pressure loss caused by die wall friction results in an inhomogeneous distribution of the relative density in the single-action die compaction. The effective pressure applied at the top end of the compact is larger than that at the bottom end, as a result of which the corresponding relative density at the top end is higher than that at the bottom end. In contrast, in the double-action die compaction, the effective pressure at both ends of the compact are larger than that in the middle region, and therefore, the relative densities in the top and bottom ends are higher. Subsequently, the densification behavior of the Cu–Al mixed metal powder in the double-action die compaction was investigated.

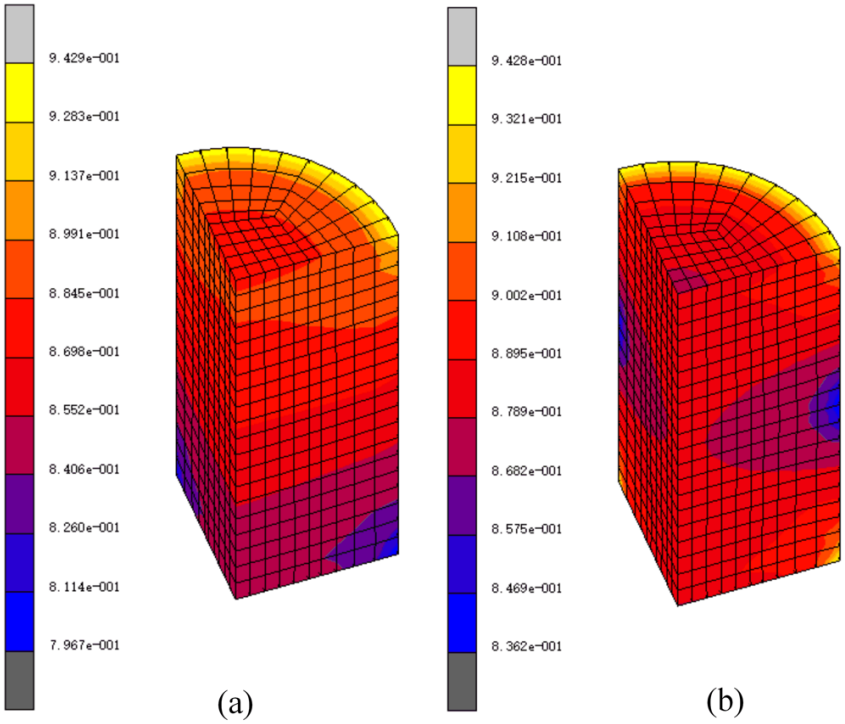

Figure 8. Comparison of the relative densities of the Cu–Al mixed metal powders during a (**a**) single-action die compaction and (**b**) double-action die compaction.

Figure 9 shows the relationship between the average relative density, ρ, of the powder compact and the compaction pressure, P, for the loose and dense initial packing structures with a different Al content. The density of a loose initial packing structure corresponds to the natural packing density of the powder under the action of gravity, and the density of a dense initial packing structure corresponds to the tap density. Our investigation results demonstrate that in both cases (i.e., loose and dense initial packing structures), a high relative density of the powder compact can be achieved as long as the compaction pressure is high enough. However, the average relative density of the compacts in the case of a dense initial packing is higher than that in the case of the loose initial packing at a given compaction pressure. It can be seen from the relative density-pressure curves that, different curves corresponding to different Al contents show the same trend, which can be considered as three compaction stages. In the first stage (P < 30 MPa), the relationship between the average relative density and the compaction pressure is nearly linear. Because the compaction pressure is too low to reach the yield limit of the powders, densification is caused mainly by the rearrangement and elastic

deformation of the powders such that the fill the voids between particles. With an increase in the compaction pressure, the average relative density increases significantly, which can be regarded as the second stage. In this stage, the compaction pressure exceeds the yield limit, which leads to the plastic deformation of particles. Therefore, the average relative density attains a high value, higher than 0.9. In the third stage, the growth trend of the average relative density is not obvious and it is starting to flatten. This is attributed to the work and hardening of particles, because of which, no further densification can occur. The trends of the curves in Figure 9 are similar to the results obtained from previous FE simulations and experiments [18,19]. These three stages accurately sum up the ρ–P curves for different Al contents, as shown in Figure 9. In addition, the relative density increases upon the addition of Al powder at a given compaction pressure.

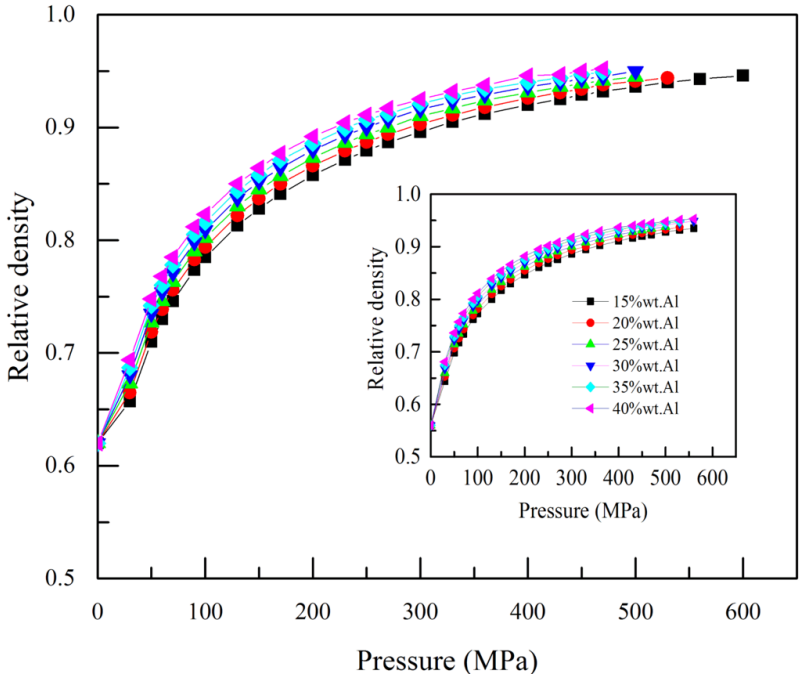

Figure 9. Evolution of average relative density with compaction pressure for dense (main plot) and loose (inset) initial packing structures.

It is known that the average relative density of the compacts with a dense initial packing is higher than that of the compacts with a loose initial packing, and thus, the properties of the compacts with these two initial packing structures are different. Figure 10 shows the relative density distributions in the powder compacts with the two different initial packing structures with an Al content of 30 wt % and the compaction pressure P of 200 MPa. It can be seen that the relative density distributions in the two compacts are similar, but the values of the relative densities are different. The relative density of the compact with the dense initial packing structure is higher than that of the compact with the loose initial packing structure, which indicates that the dense initial packing structure can provide more homogeneous and dense compacts. Subsequent simulations were performed under the condition of a dense initial packing structure.

The influence of the Al content on the relative density of the compact with a dense initial packing structure was investigated, as shown in Figure 11. Here, the compaction pressure was set as 200 MPa and Al contents of 15 wt %, 20 wt %, 25 wt %, 30 wt %, 35 wt %, and 40 wt % were considered. It can be seen that the maximum relative density is achieved at positions at the corners of the compact where it is in contact with the upper and lower punches, and the minimum relative density is achieved in the middle of the compact. Along the radial direction of the compact, the relative density decreases from the outer edge to the inner edge. The relative density in the middle region is homogeneous. Moreover,

the relative density along the axial direction on the die wall shows a symmetrical distribution. The main reason for the inhomogeneity of the relative density is the friction between the powders and the die wall. This inhomogeneity also indicates that the Al content has an impact on the local relative density distribution. With an increase in the Al content, the maximum and minimum relative densities of the compact increase. These observed trends are consistent with the literature [30].

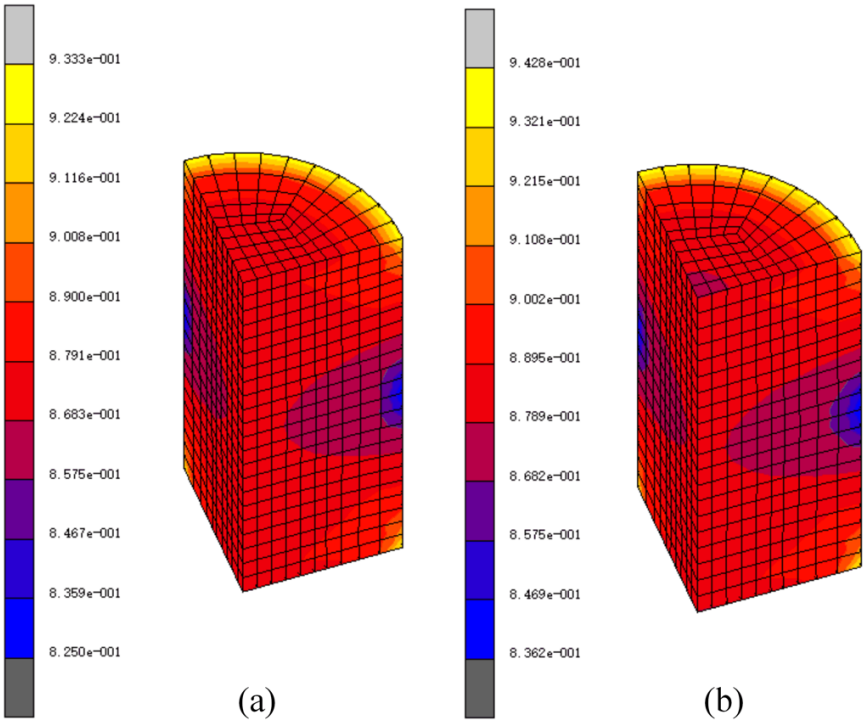

Figure 10. Relative density distribution in powder compacts with (**a**) loose initial packing structure with density $\rho_0 = 0.56$ and (**b**) dense initial packing structure with density $\rho_0 = 0.62$.

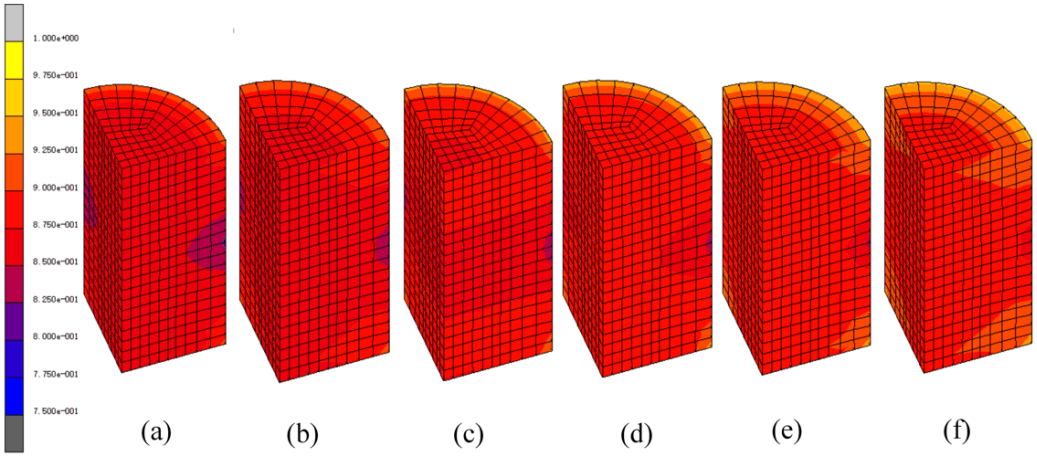

Figure 11. Relative density distributions in powder compacts at P = 200 MPa for Al contents of (**a**) 15 wt %, (**b**) 20 wt %, (**c**) 25 wt %, (**d**) 30 wt %, (**e**) 35 wt %, and (**f**) 40 wt %.

The equivalent von Mises stress distributions in the compacts with different Al contents corresponding to Figure 11 are shown in Figure 12. As can be seen in Figure 12, the maximum stress occurs in the outer layer of the compact near the punches, which is in accordance with the distribution of the relative density. The stress distribution is in agreement with previous results [31].

In addition, it is observed that the total stress of the compact decreases with the increasing Al content, which indicates a reduction in the hardness of the compact. Furthermore, the stress retention ability of the Cu powder is greater than that of the Al powder.

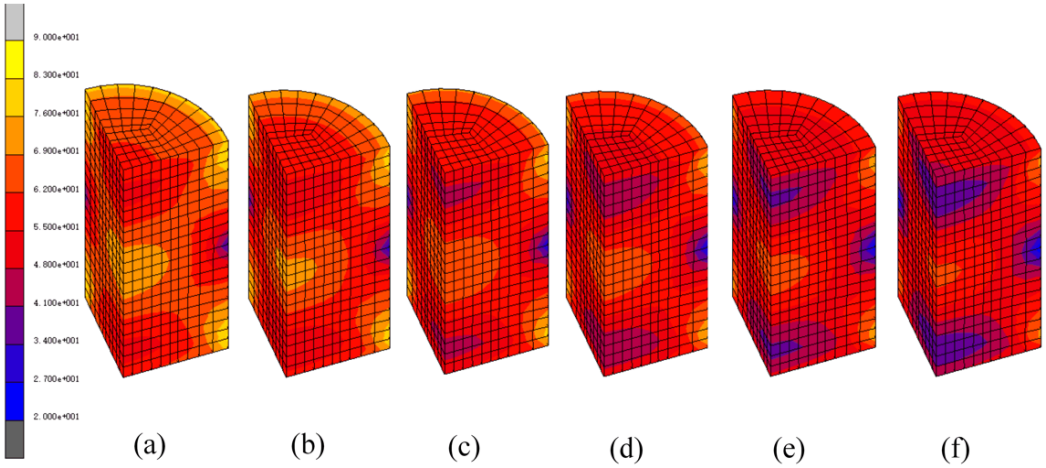

Figure 12. Equivalent von Mises stress distributions in powder compacts at P = 200 MPa for Al contents of (**a**) 15 wt %, (**b**) 20 wt %, (**c**) 25 wt %, (**d**) 30 wt %, (**e**) 35 wt %, and (**f**) 40 wt %.

3.2. Effect of Compaction Pressure

The evolution of the average relative density with compaction pressure, as shown in Figure 5, illustrates that the compaction pressure has an obvious influence on the properties of the compact. Therefore, the internal characteristics of the compact are different at different compaction pressures. The effects of various compaction pressures, 100 MPa, 150 MPa, 200 MPa, 250 MPa, and 300 MPa, on the internal characteristics of the compact were investigated at an Al content of 30 wt %. Figure 13 shows the relative density distributions in the compacts subjected to the different compaction pressures; here, each compact corresponds to a different compaction pressure. As it can be seen from this figure, the relative density distributions are similar to those in Figure 11. The highest relative density is achieved at the top and bottom corners of the powder compact, whereas the lowest relative density is achieved in the middle region of the compact, close to the die wall. In addition, the overall relative density increases with the increasing compaction pressure, and the density gradient decreases gradually.

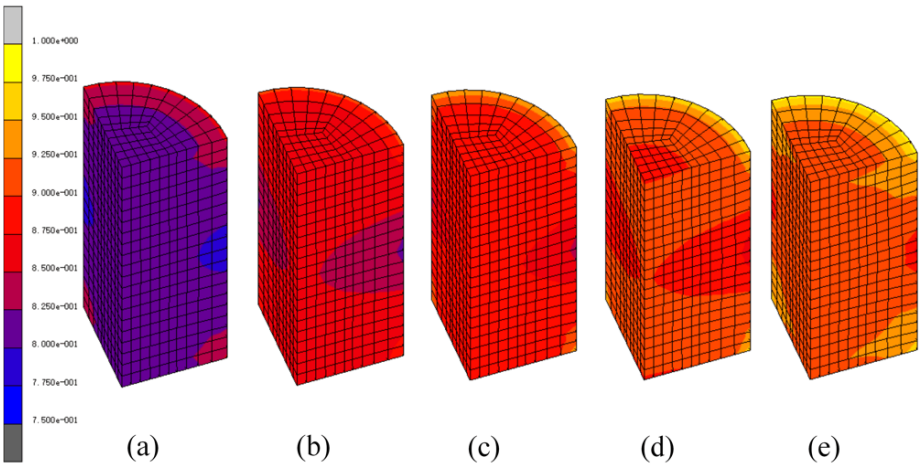

Figure 13. Relative density distributions in the powder compacts with an Al content of 30 wt % at compaction pressures, P, of (**a**) 100 MPa, (**b**) 150 MPa, (**c**) 200 MPa, (**d**) 250 MPa, and (**e**) 300 MPa.

The trend of the equivalent von Mises stress distribution at various compaction pressures in Figure 14 is contrary to that in Figure 12. The overall stress increases with the increasing compaction pressure. However, the equivalent von Mises stress distribution in each compact is similar to that in Figure 12. When the compaction pressure is 100 MPa, the stress distribution and the relative density distribution are remarkably similar. The highest stress occurs in the corner regions with the highest relative density, and the lowest stress occurs in the regions with the lowest relative density.

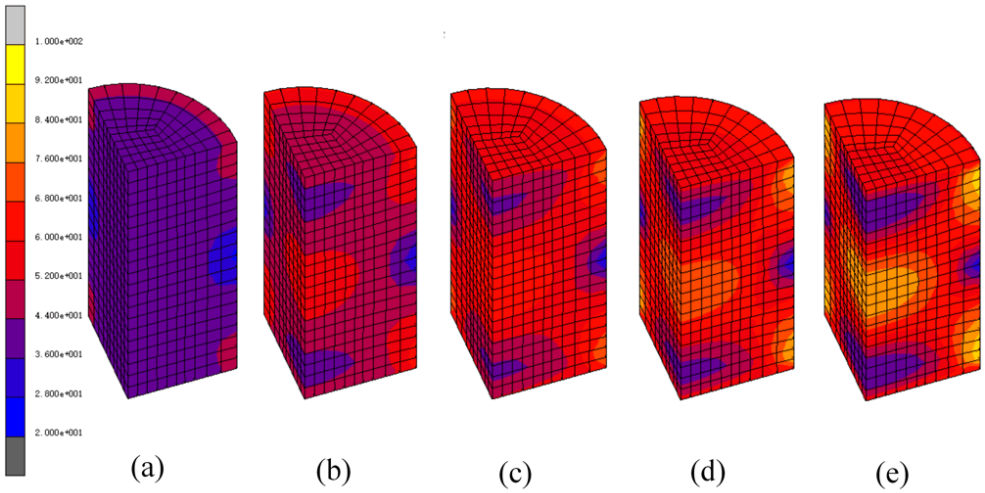

Figure 14. Equivalent von Mises stress distributions in the powder compacts with an Al content of 30 wt % at a compaction pressure, *P*, of (**a**) 100 MPa, (**b**) 150 MPa, (**c**) 200 MPa, (**d**) 250 MPa, and (**e**) 300 MPa.

3.3. Effect of Die Wall Friction on Densification Behavior

Through the above-mentioned analysis, it can be seen that both the relative density gradient and the stress gradient exist in the powder compact, which can be attributed to the behavior of the powder flow. However, the friction between the die wall and the powders is the main reason for a restricted powder flow. Therefore, the influence of different friction conditions on the densification behavior at an Al content of 30 wt % was investigated. Figure 15 shows the variation of the average relative density with the compaction pressure at different die wall friction coefficients. It can be seen that the average relative density decreases with the increasing die wall friction coefficient. To assess the influence of the die wall friction on the densification behavior of the Cu–Al mixed metal powder, the Van Der Zwan–Siskens empirical compaction equations were applied, and the fitting parameters are shown in Table 2. The curves of variation of parameters *A* and *B* in the Van Der Zwan–Siskens compaction equation with the friction coefficient were fitted, these curves are shown in Figure 16. Consequently, the compaction equation of the Cu–Al mixed metal powder, including the effect of die wall friction can be expressed as follows:

$$\frac{\rho - \rho_0}{\rho(1-\rho_0)} = (-0.17529\mu + 1.02591)\exp\left(\frac{-38.55605\mu - 38.76326}{P}\right) \quad (18)$$

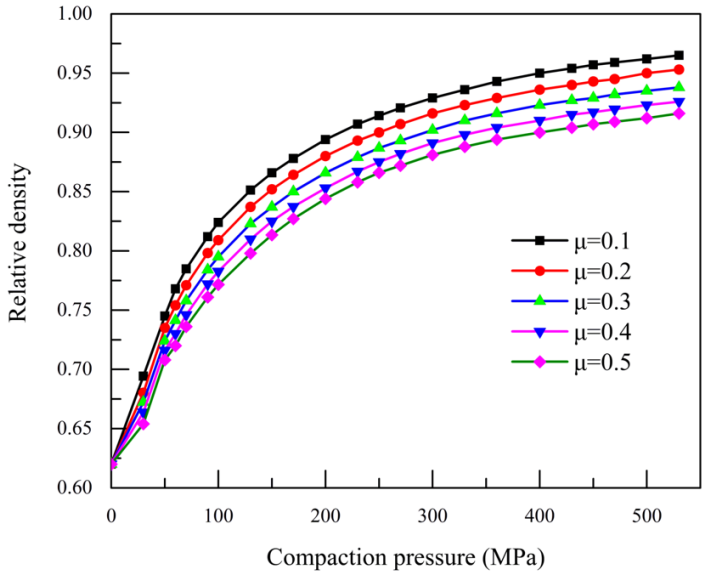

Figure 15. Evolution of the average relative density with compaction pressure at different die wall friction coefficients.

Table 2. Fitting parameters of Van Der Zwan–Siskens equation with different die wall friction coefficients.

Van Der Zwan–Siskens Equation: $\frac{\rho-\rho_0}{\rho(1-\rho_0)} = A_4 \exp(\frac{B_4}{P})$			
μ	A_4	B_4	R^2
0.1	1.01041	−42.81596	0.9963
0.2	0.99003	−46.29819	0.99694
0.3	0.97149	−50.23743	0.99694
0.4	0.95375	−54.11138	0.99729
0.5	0.94091	−58.18739	0.99748

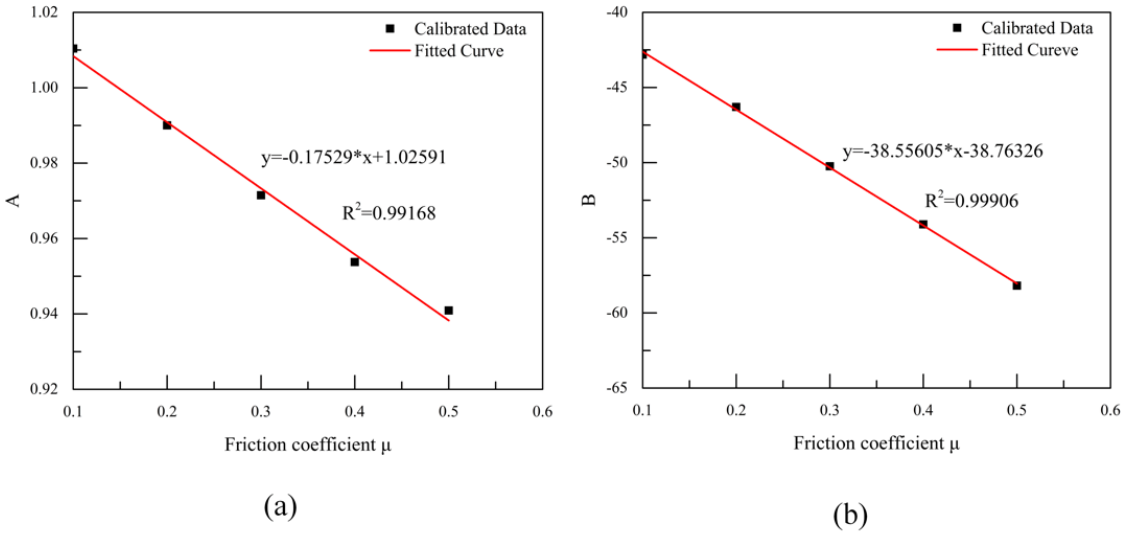

Figure 16. Fitting curves of parameters in Van Der Zwan–Siskens compaction equation: (**a**) parameter *A* and (**b**) parameter *B*.

In general, different friction conditions result in different compact properties. The relative density distribution in the compacts at different die wall friction coefficients (μ = 0.05, μ = 0.2, and μ = 0.4) is shown in Figure 17. This figure reveals that the density distributions in the compacts are similar, but that the values of the relative densities of the compacts are different. The largest differences in the relative densities at these three die wall friction coefficients are 0.0283, 0.1066, and 0.1934, respectively, indicating that the die wall friction has a significant influence on the properties of the compact, and that the relative density gradient increases with the increasing die wall friction coefficient. Figure 18 shows the corresponding equivalent von Mises stress distributions, the values of the von Mises stress are in the ranges of 47.94–63.87 MPa, 24.28–76.59 MPa, and 20.59–87.94 MPa, for μ = 0.05, μ = 0.2, and μ = 0.4, respectively. The difference in stress within the compact is observed to be large, indicating that the die wall friction has a severe impact on the stress distribution and that it is the main factor inducing the stress gradient in the powder compact [19].

The density gradient is generated by the powder movement, and the die wall friction has an obvious effect on the powder flow. Simultaneous powder flow in the axial and radial direction occurs in the die. The axial displacement distributions and the curves of variation of the axial displacement with the radial distance at different compact heights under different friction conditions are shown in Figures 19–21. Five positions (i.e., heights), H = 4 mm, H = 12 mm, H = 20 mm, H = 28 mm, and H = 36 mm, were considered for the analysis. The minus sign "−" in the displacement curves represents a powder flow direction opposite to the coordinate axis. Figures 19a, 20a and 21a show the axial displacement distributions, and it can be seen that the powder flow in double-action die compaction is symmetrical. The absolute value of the axial displacement in the upper half of the compact is equal to that in the corresponding lower half. Furthermore, the axial displacements in the top and bottom regions of the compact are larger than that in the middle region, indicating that the axial load is transmitted from both ends to the middle region. Figures 19b, 20b and 21b show the curves of variation of the axial displacement with the radial distance at five different compact heights, under three friction conditions (μ = 0.05, μ = 0.2, and μ = 0.4, respectively). Under these three friction conditions, the trends of axial flow are similar, but the values of the axial displacement are different. The powder close to the punches has large displacement. The closer the powder to the middle region of the compact, the smaller the axial displacement will be. The axial displacement is almost 0 at H = 20 mm. It is also observed that when the die wall friction coefficient is 0.05, the axial displacement in the middle region and that near the die wall are almost the same at all of the compact heights. However, in the other two cases (i.e., μ = 0.2 and μ = 0.4), the axial displacements are noticeably different. Therefore, the die wall friction has a significant effect on the powder flow. It can be concluded that, by increasing the die wall friction coefficient, the axial displacements decrease and the axial displacement gradient becomes more prominent. Figure 22 shows the radial displacement distribution in the compact, under three different friction conditions. It can be observed that convective flow exists in the powder compact. The radial powder flow can be divided into two types corresponding to the positive and negative signs of the distribution, an inward flow that is opposite to the X-coordinate axis and an outward flow that is along the X-coordinate axis. The powder near the top and bottom punches flows to the central of the compact, while the powder in the middle part flows to the die wall. The radial displacement in the upper half and lower half of the compact are completely equal, in terms of both the value and the flow direction. Furthermore, the middle region of the compact shows the largest radial displacement. In addition, the radial displacement increases with increasing die wall friction coefficient. However, the radial displacement is so small that it has a negligible effect on the powder compaction process in comparison to the axial displacement.

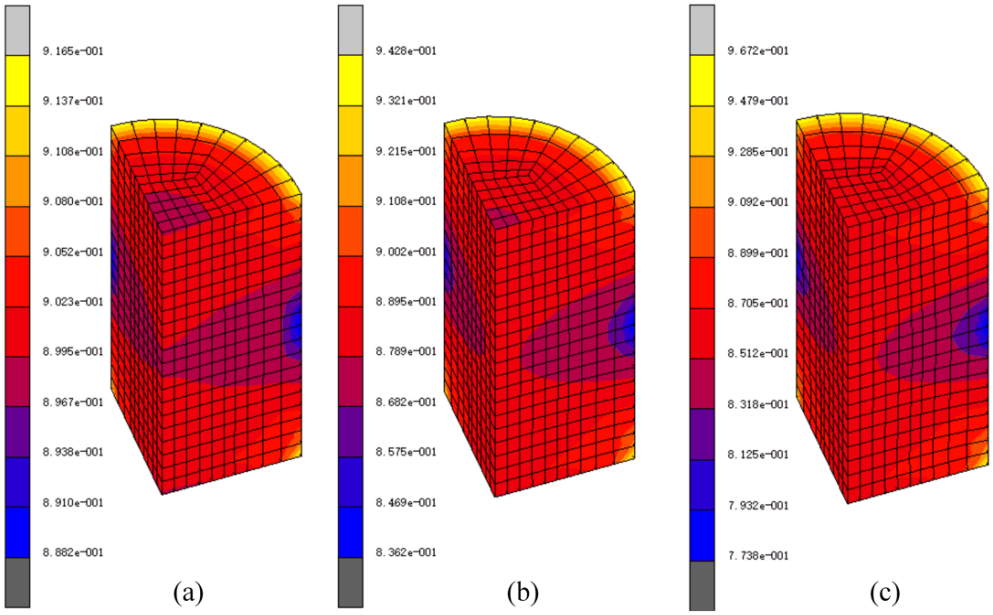

Figure 17. Relative density distributions in compacts at different μ values of (**a**) 0.05, (**b**) 0.2, and (**c**) 0.4.

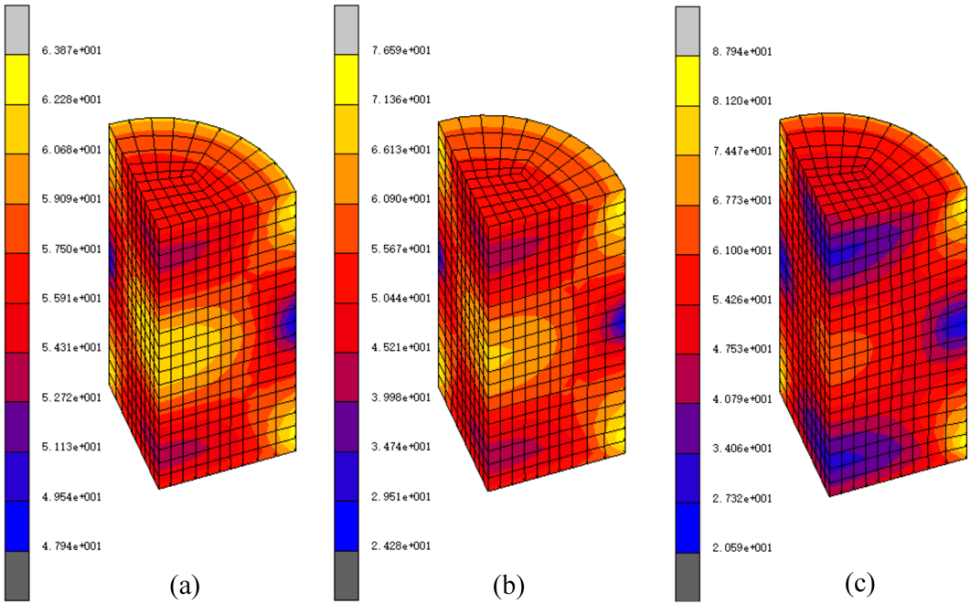

Figure 18. Equivalent von Mises stress distributions in powder compacts at different μ values of (**a**) 0.05, (**b**) 0.2, and (**c**) 0.4.

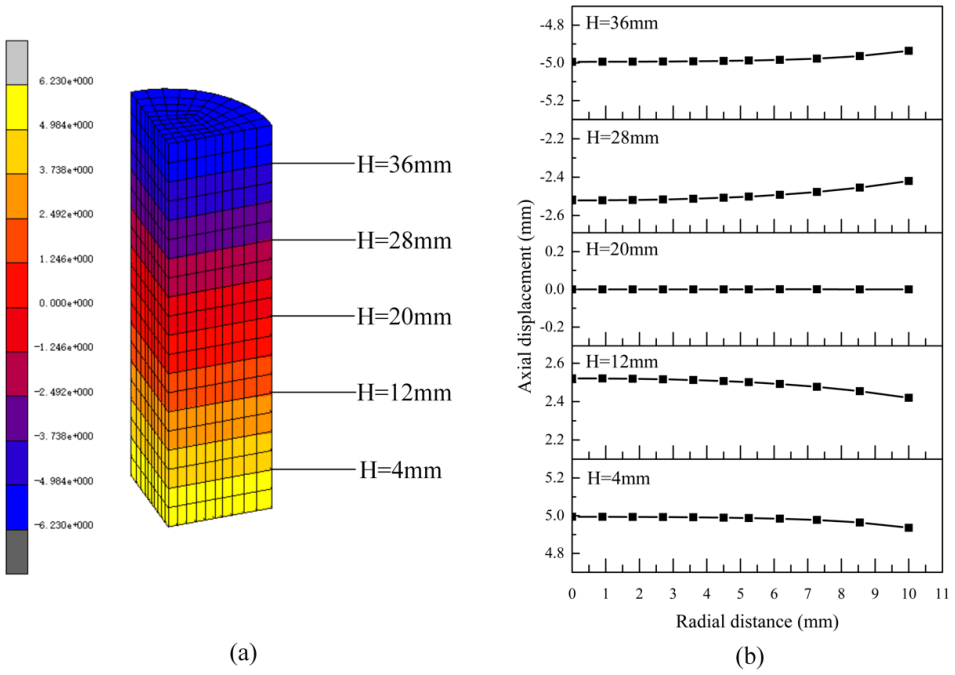

Figure 19. Axial displacement distribution in powder compact at μ = 0.05 in (**a**) displacement contours and (**b**) displacement at different compact heights.

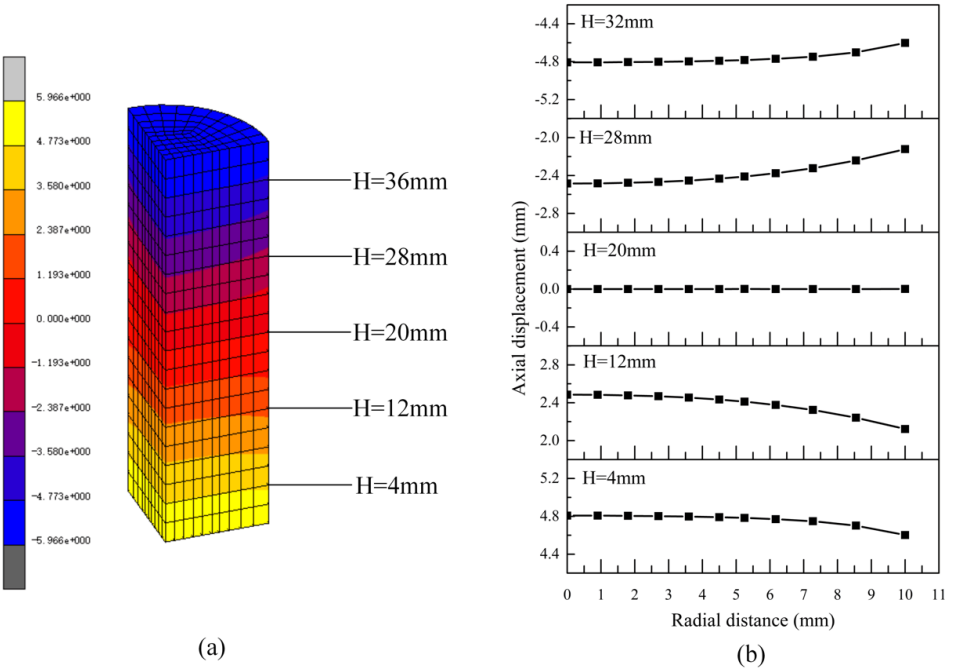

Figure 20. Axial displacement distribution in powder compact at μ= 0.2 in (**a**) displacement contours and (**b**) displacement at different compact heights.

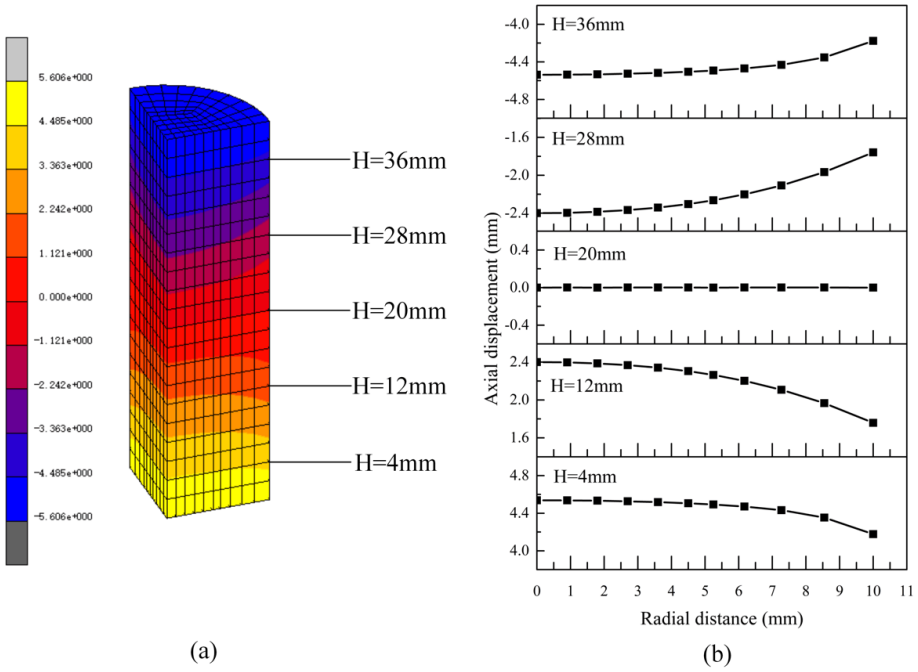

Figure 21. Axial displacement distribution in powder compact at μ= 0.4 in (**a**) displacement contours and (**b**) displacement at different compact heights.

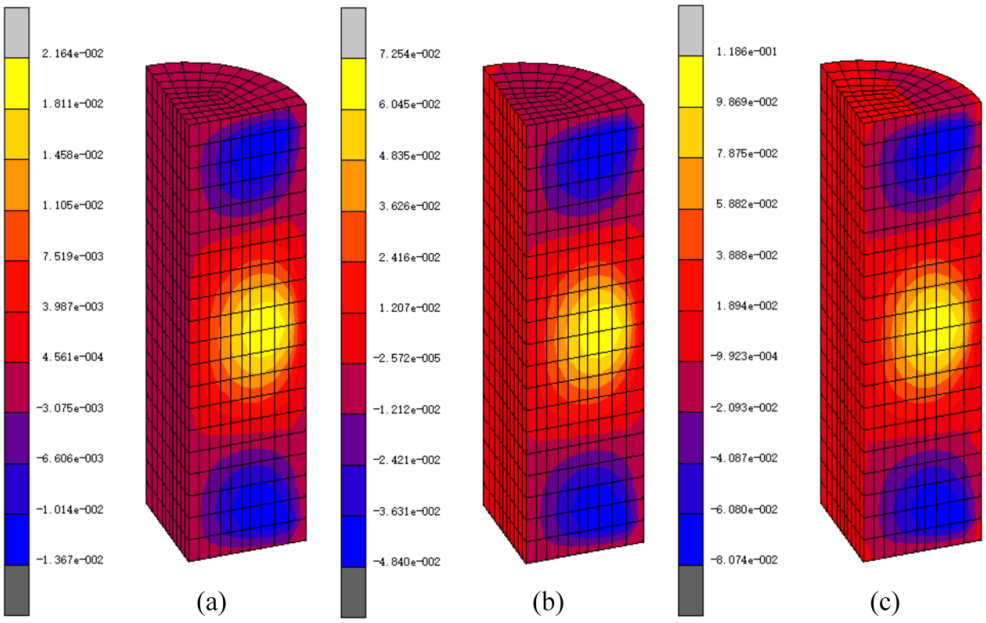

Figure 22. Radial displacement distributions in powder compact at different μ values at (**a**) 0.05, (**b**) 0.2, and (**c**) 0.4.

3.4. Effect of Dwell Time on Densification Behavior

In addition to the effects of the initial packing density, the Al content, compaction pressure, and die wall friction on the double-action die compaction of the mixed metal powders, the effect of the dwell time on the compact properties was also analyzed. Figure 23 shows the evolution of the average relative density with the compaction pressure for different dwell times at an Al content of 30 wt % and a friction coefficient of 0.2. It can be observed that the average relative density increases with the increasing dwell time. The average relative density is 0.876 when the compaction pressure is 600 MPa

and the dwell time is 0; in contrast, the average relative density is 0.96 when dwell time is 15 min, which corresponds to a 9.6% improvement.

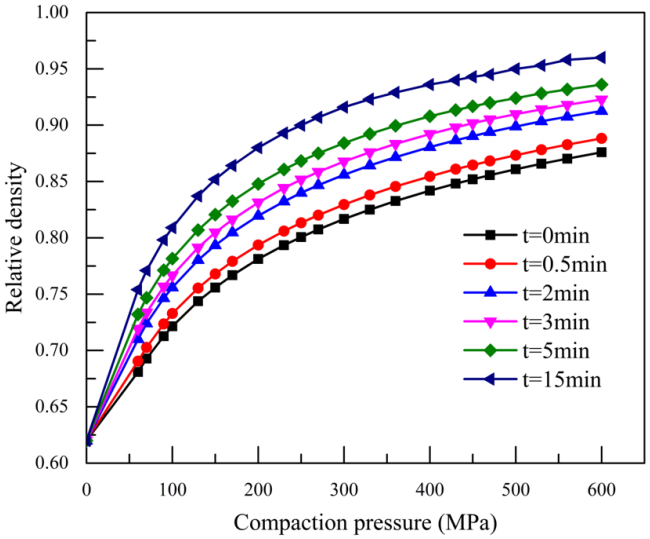

Figure 23. Evolution of average relative density with compaction pressure for different dwell times.

The relative density distribution in the compact for four different dwell times was simulated, as shown in Figure 24. The simulation results show that the dwell time has a significant influence on the compact properties. As the dwell time increases, the relative density of the compact increases and becomes more homogeneous. This is because the compaction pressure is completely transferred to the compact when the dwell times are longer, which, in turn, increases the relative density distribution in all of the regions of the compact. Furthermore, the air present in the powder voids has sufficient time to escape from the gap between the die wall and the punches. Furthermore, the pressure retention permits the mechanical meshing of the powders and their deformation, which contributes to the process of strain relaxation. Figure 25 shows the equivalent von Mises stress distribution in the compact for the different dwell times. It is observed that the equivalent von Mises stress decreases with the increasing dwell time, which indicates that the dwell time affects the stress distribution and a longer dwell time is conducive to densification.

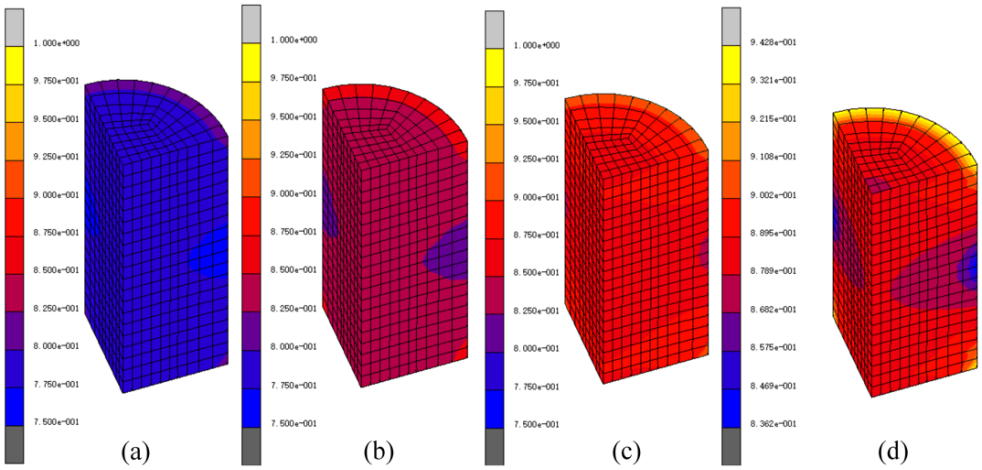

Figure 24. Relative density distributions in compact at compaction pressure of 200 MPa and for various dwell times at (**a**) t = 0 min, (**b**) t = 3 min, (**c**) t = 10 min, and (**d**) t = 15 min.

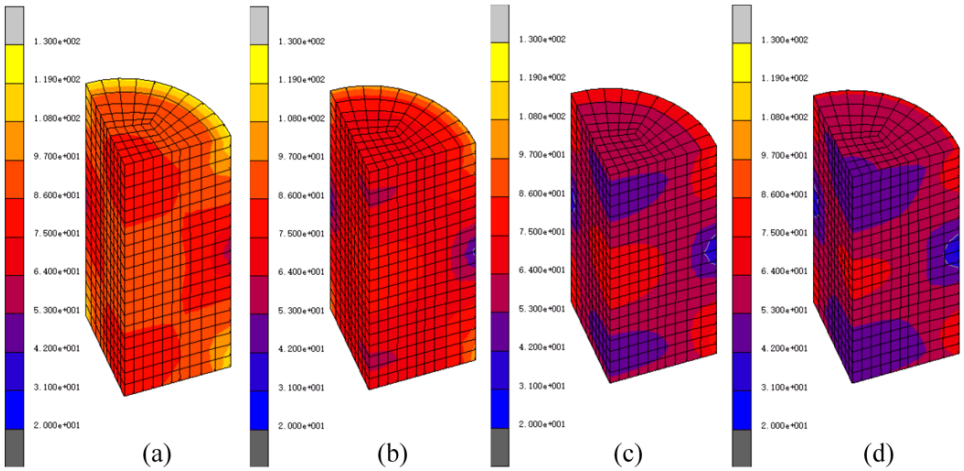

Figure 25. Equivalent von Mises stress distributions in compact at a compaction pressure of 200 MPa for various dwell times at (**a**) t = 0 min, (**b**) t = 3 min, (**c**) t = 10 min, and (**d**) t = 15 min.

3.5. Analysis of Height–Diameter Ratio

To investigate the effect of the height–diameter (H/D) ratio on the powder compact, five different initial powder heights, H0 = 20 mm, H0 = 30 mm, H0 = 40 mm, H0 = 50 mm, and H0 = 60 mm, were considered for the analysis. These heights ensured that the H/D ratio of the green compacts pressed at 200 MPa was 0.7, 1, 1.4, 1.8, and 2.12, respectively. As shown in Figure 26, the relative density distribution in the compact for five different H/D ratios was simulated. The figure reveals that the density distributions in the compacts are similar, but that the values of the relative densities of the compacts are different. The lowest relative density lies in the middle of the compact decreases, with an increasing H/D ratio. And the largest differences in the relative densities are 0.0851, 0.0987, 0.1066, 0.1142, and 0.1206, respectively, indicating that the relative density gradient increases with the increasing H/D ratio, and the relative density distribution becomes non-uniform. Figure 27 shows the corresponding equivalent von Mises stress distributions; it can be seen that, with the increasing of H/D ratio, the low stress region increases and the distribution of stress is more heterogeneous.

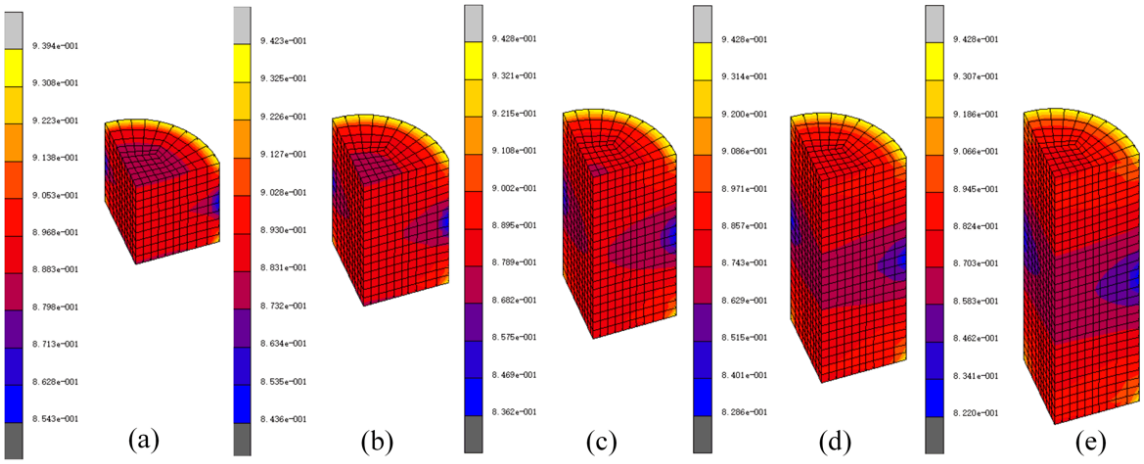

Figure 26. Relative density distributions in compact at the compaction pressure of 200 MPa for various height–diameter (H/D) ratios of (**a**) H/D = 0.7, (**b**) H/D = 1, (**c**) H/D = 1.4, (**d**) H/D = 1.8, and (**e**) H/D = 2.12.

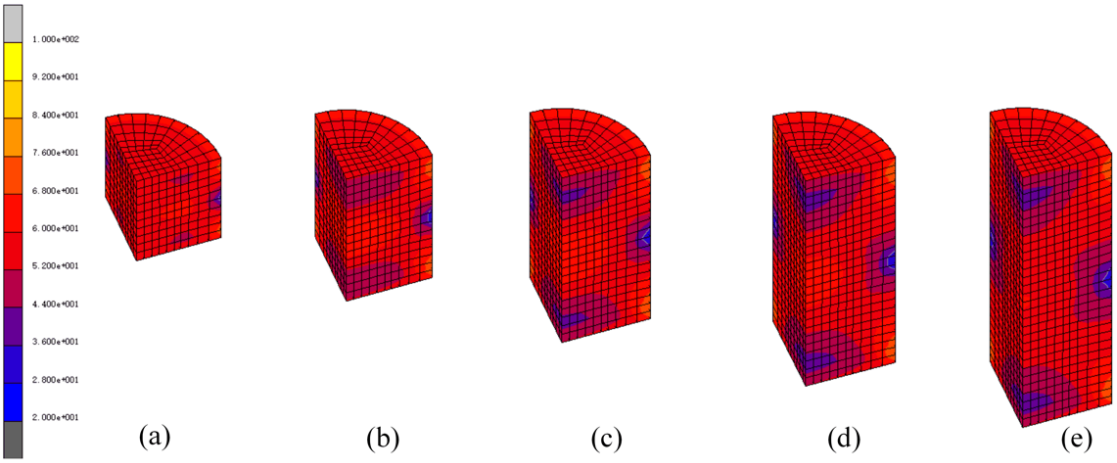

Figure 27. Equivalent von Mises stress distributions in compact at the compaction pressure of 200 MPa for H/D ratios of (**a**) H/D = 0.7, (**b**) H/D = 1, (**c**) H/D = 1.4, (**d**) H/D = 1.8, and (**e**) H/D = 2.12.

For the powder with a higher initial packing height, the friction between the powder and the die wall is higher. Therefore, the pressure lost increases in the process of the powder compaction, and the middle region of the compact has the lowest density. With the increasing H/D ratio, the relative density gradient increases and the average relative density decreases, as shown in Figure 28. Therefore, the high H/D ratio is negative for the properties of compact.

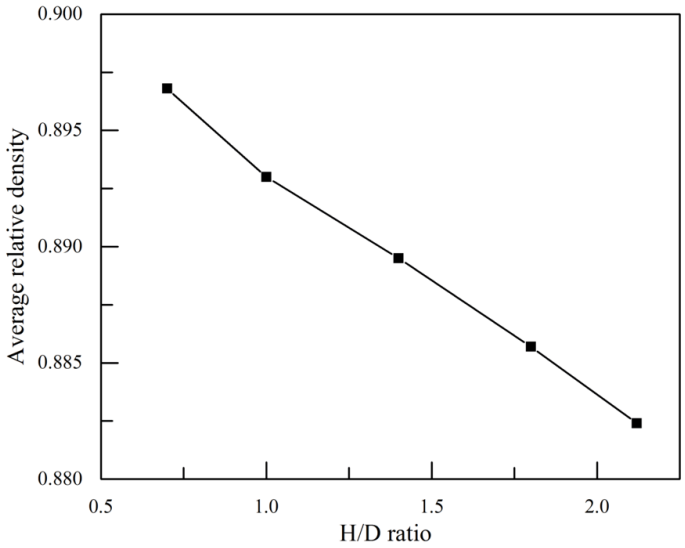

Figure 28. Variation of average relative density with H/D ratio.

3.6. Analysis of Spring Back after Ejection

The last step in the powder compaction is the ejection from the mold, in which a spring-back of the compact occurs. This spring-back is caused by the elastic expansion of the compact. Owing to the elastic and plastic deformations of the powder particles, excessive internal elastic stress is generated in the compact and its direction is opposite to that of the external forces acting on the particles, so as to prevent the deformation. When the compaction pressure is removed from compact, the internal elastic stress relaxes, and so the particle shape and the contact state between the particles change; this results in swelling of the powder compact. Several factors affect the spring-back of the compact, such as the

particle size, particle shape, and compaction pressure. The spring-back of the compact is characterized as the percentage of expansion, and is expressed as follows:

$$\delta = \Delta l / l_0 \times 100\% = [(l - l_0)/l_0] \times 100\% \quad (19)$$

where δ is the residual elasticity along the height or diameter of the compact, l_0 is the height or diameter of the compact before ejection, and l is the height or diameter of the compact after ejection. Figure 29 shows the curve of variation of the axial residual elasticity with the compaction pressure at an Al content of 30 wt %. It can be seen that the axial residual elasticity increases with the increasing compaction pressure. The internal elastic stress increases with the increasing compaction pressure; therefore, the spring-back of the compacts becomes more obvious with the increasing compaction pressure. Furthermore, the spring-back of the compact is anisotropic. Meanwhile, the axial pressure is larger than the radial pressure, as a result of which the axial residual elasticity is higher than the radial residual elasticity [18].

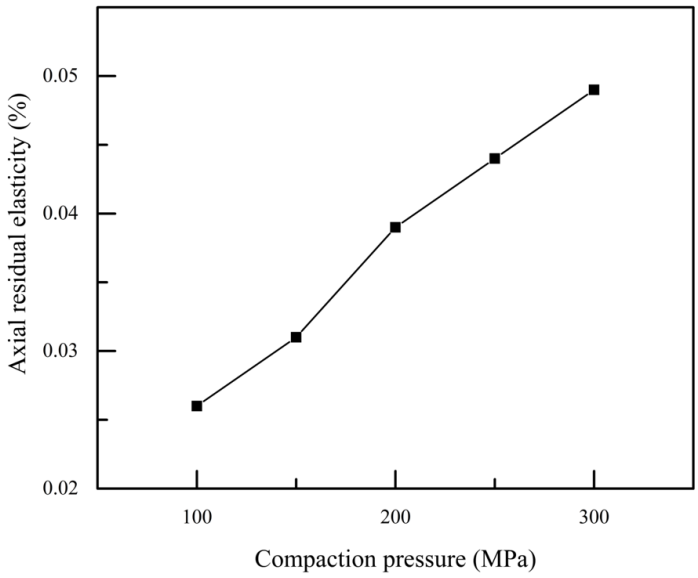

Figure 29. Curve of variation of axial residual elasticity with compaction pressure.

4. Conclusions

The densification mechanism of the Cu–Al mixed metal powders subjected to double-action die compaction was numerically simulated by the finite element method. Firstly, the single-action die compaction was compared with the double-action die compaction to demonstrate that the latter is more effective than the former in producing high-performance compacts. It is validated by numerical and experiment results. Then, two different initial packing structures were compared and simulated to investigate the influence of the initial packing structure on the properties of the compacts. It was observed that even though a sufficiently high compaction led to almost fully dense compacts in both cases, more uniform relative density and stress distributions were achieved in the case of dense initial packing structures at a low compaction pressure. Furthermore, the Al content was found to have a significant effect on the properties of the compacts. With an increase in the Al content, the relative density increased, whereas the equivalent von Mises stress decreased. Under the condition of a fixed Al content and an initial packing structure, the relative density and stress increased with the increasing compaction pressure.

Furthermore, the influence of the die wall friction on the densification behavior of the composite powder was investigated, based on the Van Der Zwan–Siskens compaction equation. The equation is used for the analysis of the compaction behavior of Cu–Al 30 wt % composite powder. A fitted

equation that included the effect of the die wall friction was proposed; this equation is expressed as $\frac{\rho-\rho_0}{\rho(1-\rho_0)} = (-0.17529\mu + 1.02591)\exp(\frac{-38.55605\mu-38.76326}{P})$. However, the relative density and stress distributions were mainly a result of the radial powder flow, and the radial displacement gradient became more significant with increasing die wall friction coefficient.

Finally, the effects of the dwell time on the compaction behavior were analyzed. The results revealed that the overall average relative density increased and the stress decreased with the increasing dwell time, indicating that an appropriate dwell time would promote densification. Further analysis was performed to investigate the H/D ratio effect. The results showed that a high H/D ratio decreased the densification rate and that the average relative density decreased with the increasing H/D ratio. At last, the spring-back after the ejection was performed. The analysis showed that the higher the compaction pressure, the more obvious the spring-back of the compact will be.

Author Contributions: W.W., H.Q., and P.L. conceived the finite element model, and W.W., Y.Z., and H.C. conducted the numerical modeling research. All of the authors discussed the results and worked together on preparing the manuscript.

Acknowledgments: This work was supported by the National Natural Science Foundation of Heilongjiang Province, China (No. A201404) and by the Fundamental Research Funds of Harbin Engineering University (No. HEUCFP201780).

Conflicts of Interest: The authors declare no conflict of interest.

References

1. Gohar, G.A.; Manzoor, T.; Shah, A.N. Investigation of thermal and mechanical properties of Cu-Al alloys with silver addition prepared by powder metallurgy. *J. Alloys Compd.* **2018**, *735*, 802–812. [CrossRef]
2. Makhlouf, M.B.; Bachaga, T.; Sunol, J.J.; Dammak, M.; Khitouni, M. Synthesis and Characterization of Nanocrystalline Al-20 at. % Cu Powders Produced by Mechanical Alloying. *Metals* **2016**, *6*, 145. [CrossRef]
3. Celik, F.A. Pressure and cooling rate effect on polyhedron clusters in Cu-Al alloy by using molecular dynamics simulation. *Phys. B-Condens. Matter* **2014**, *450*, 71–76. [CrossRef]
4. Dudina, D.V.; Lomovsky, O.I.; Valeev, K.R.; Tikhov, S.F.; Boldyreva, N.N.; Salanov, A.N.; Cherepanova, S.V.; Zaikovskii, V.I.; Andreev, A.S.; Lapina, O.B.; et al. Phase evolution during early stages of mechanical alloying of Cu–13 wt.% Al powder mixtures in a high-energy ball mill. *J. Alloys Compd.* **2015**, *629*, 343–350. [CrossRef]
5. Kim, J.S.; Jiang, K.; Chang, I. A net shape process for metallic microcomponent fabrication using Al and Cu micro/nano powders. *J. Micromech. Microeng.* **2006**, *16*, 48–52. [CrossRef]
6. Kim, S.H.; Noh, S.H.; Kim, S.M.; Sung, S.Y.; Jin, J.K.; Kim, S.M. Fabrication of porous Al-Cu sintered body and its permeability property. *Korean J. Met. Mater.* **2014**, *52*, 783–789. [CrossRef]
7. Lim, A.B.Y.; Long, X.; Shen, L.; Chen, X.; Ramanujan, R.V.; Gan, C.L.; Chen, Z. Effect of palladium on the mechanical properties of Cu–Al intermetallic compounds. *J. Alloys Compd.* **2015**, *628*, 107–112. [CrossRef]
8. Saiprasad, M.; Atchayakumar, R.; Thiruppathi, K.; Raghuraman, S. Consolidation of copper and aluminium powders by spark plasma sintering. *IOP Conf. Ser. Mater. Sci. Eng.* **2016**, *149*, 012057. [CrossRef]
9. Dias, A.N.O.; Silva, A.D.; Rodrigues, C.A.; Melo, M.d.L.N.M.; Rodrigues, G.; Silva, G. Effect of high energy milling time of the aluminum bronze alloy obtained by powder metallurgy with niobium carbide addition. *Mater. Res.* **2017**, *20*, 747–754. [CrossRef]
10. Yin, Z.; Sun, L.L.; Yang, J.; Gong, Y.L.; Zhu, X.K. Mechanical behavior and deformation kinetics of gradient structured Cu-Al alloys with varying stacking fault energy. *J. Alloys Compd.* **2016**, *687*, 152–160. [CrossRef]
11. Tokita, M. Trends in Advanced SPS Sparek Plasma Sintering Systems and Technology. *J. Res. Assoc. Powder Technol. Jpn.* **1993**, *30*, 790–804. [CrossRef]
12. Tian, Y.Z.; Zhao, L.J.; Park, N.; Liu, R.; Zhang, P.; Zhang, Z.J.; Shibata, A.; Zhang, Z.F.; Tsuji, N. Revealing the deformation mechanisms of Cu–Al alloys with high strength and good ductility. *Acta Mater.* **2016**, *110*, 61–72. [CrossRef]
13. Ning, J.L.; Wang, D. Concurrent high strength and high ductility in isotropic bulk Cu–Al alloy with three-dimensional nano-twinned structure. *J. Alloys Compd.* **2012**, *514*, 214–219. [CrossRef]
14. Chakravarty, S.; Sikdar, K.; Singh, S.S.; Roy, D.; Koch, C.C. Grain size stabilization and strengthening of cryomilled nanostructured Cu 12 at% Al alloy. *J. Alloys Compd.* **2017**, *716*, 197–203. [CrossRef]

15. Wolla, D.W.; Davidson, M.J.; Khanra, A.K. Studies on the formability of powder metallurgical aluminum–copper composite. *Mater. Des.* **2014**, *59*, 151–159. [CrossRef]
16. Li, H.X.; Tian, B.H.; Lin, Y.M.; Li, S.K.; Liu, P. Recrystallization behavior of Al_2O_3/Cu composite produced by internal oxidation. *Rare Met. Mater. Eng.* **2005**, *34*, 1039–1042.
17. An, X.Z.; Xing, Z.T.; Jia, C.C. Cold Compaction of Copper Powders Under Mechanical Vibration and Uniaxial Compression. *Metall. Mater. Trans. A* **2014**, *45A*, 2171–2179. [CrossRef]
18. An, X.Z.; Zhang, Y.L.; Zhang, Y.X.; Yang, S. Finite Element Modeling on the Compaction of Copper Powder Under Different Conditions. *Metall. Mater. Trans. A* **2015**, *46A*, 3744–3752. [CrossRef]
19. Zhou, M.C.; Huang, S.Y.; Hu, J.H.; Lei, Y.; Zou, F.; Yan, S.; Yang, M. Experiment and finite element analysis of compaction densification mechanism of Ag-Cu-Sn-In mixed metal powder. *Powder Technol.* **2017**, *313*, 68–81. [CrossRef]
20. Shima, S.; Oyane, M. Plasticity theory for porous metals. *Int. J. Mech. Sci.* **1976**, *18*, 285–291. [CrossRef]
21. Kuhn, H.A.; Downey, C.L. Deformation characteristics and plasticity theory of sintered powder materials. *Int. J. Powder Metall.* **1971**, *7*, 15–25.
22. Doraivelu, S.M.; Gegel, H.L.; Gunasekera, J.S.; Malas, J.C.; Morgan, J.T.; Thomas, J.F. A new yield function for compressible PM materials. *Int. J. Mech. Sci.* **1984**, *26*, 527–535. [CrossRef]
23. Ghita, C.; Popescu, I.N. Experimental research and compaction behaviour modelling of aluminium based composites reinforced with silicon carbide particles. *Comput. Mater. Sci.* **2012**, *64*, 136–140. [CrossRef]
24. Han, P.; An, X.Z.; Zhang, Y.X.; Zou, Z.S. FEM Modeling of the Compaction of Fe and Al Composite Powders. *J. Min. Metall. Sect. B-Metall.* **2015**, *51*, 163–171. [CrossRef]
25. Zhdanovich, G.M.; Sidorov, V.A.; Yakubovskii, C.A. Distribution of pressure and density in powder compacts of complex configuration. *Sov. Powder Metall. Met. Ceram.* **1982**, *21*, 441–446. [CrossRef]
26. Heckel, R.W. Density-pressure relationships in powder compaction. *Trans. Metall. Soc. AIME* **1961**, *221*, 671–675.
27. Huang, P.Y.; Jin, Z.P.; Chen, Z.H. *Basic Theory and New Technology of Powder Metallurgy*; Science Press: Beijing, China, 2010; pp. 21–23.
28. Balshin, M.Y. Theory of compacting. *V. Metalloprom* **1938**, *18*, 124–137.
29. Sivasankaran, S.; Sivaprasad, K.; Narayanasamy, R.; Iyer, V.K. Evaluation of compaction equations and prediction using adaptive neuro-fuzzy inference system on compressibility behavior of AA 6061100-x-x wt.% TiO_2 nanocomposites prepared by mechanical alloying. *Powder Technol.* **2011**, *209*, 124–137. [CrossRef]
30. Van der Zwan, J.; Siskens, A.M. The compaction and mechanical properties of agglomerated materials. *Powder Technol.* **1982**, *33*, 43–54. [CrossRef]
31. Abedinzadeh, R.; Safavi, S.M.; Karimzadeh, F. Finite Element modeling of Microwave-Assisted Hot Press process in a multimode furnace. *Appy. Math. Model.* **2015**, *39*, 7452–7468. [CrossRef]